

***A WATER-BASED FAST INTEGRATED MOBILITY
SPECTROMETER (WFIMS) WITH ENHANCED
DYNAMIC SIZE RANGE***

Pinterich, T., Spielman, S. R., Hering, S., and Wang, J. A.

*Accepted for publication in
Aerosol Science and Technology*

June 2017

**Environmental & Climate Science Dept.
Brookhaven National Laboratory**

**U.S. Department of Energy
DOE Office of Science**

Notice: This manuscript has been authored by employees of Brookhaven Science Associates, LLC under Contract No. DE-SC0012704 with the U.S. Department of Energy. The publisher by accepting the manuscript for publication acknowledges that the United States Government retains a non-exclusive, paid-up, irrevocable, world-wide license to publish or reproduce the published form of this manuscript, or allow others to do so, for United States Government purposes.

This preprint is intended for publication in a journal or proceedings. Since changes may be made before publication, it may not be cited or reproduced without the author's permission.

DISCLAIMER

This report was prepared as an account of work sponsored by an agency of the United States Government. Neither the United States Government nor any agency thereof, nor any of their employees, nor any of their contractors, subcontractors, or their employees, makes any warranty, express or implied, or assumes any legal liability or responsibility for the accuracy, completeness, or any third party's use or the results of such use of any information, apparatus, product, or process disclosed, or represents that its use would not infringe privately owned rights. Reference herein to any specific commercial product, process, or service by trade name, trademark, manufacturer, or otherwise, does not necessarily constitute or imply its endorsement, recommendation, or favoring by the United States Government or any agency thereof or its contractors or subcontractors. The views and opinions of authors expressed herein do not necessarily state or reflect those of the United States Government or any agency thereof.

A Water-based Fast Integrated Mobility Spectrometer (WFIMS) with enhanced dynamic size range

Running Head: A Water-based Fast Integrated Mobility Spectrometer

Tamara Pinterich¹, Steven R. Spielman², Susanne Hering², Jian Wang^{1,*}

¹Brookhaven National Laboratory, Upton, NY-11973-5000, USA

²Aerosol Dynamics Inc., Berkeley, CA-94710, USA

*Corresponding author mail: jian@bnl.gov

Abstract

A Water-based Fast Integrated Mobility Spectrometer (WFIMS) with enhanced dynamic size range is developed. The WFIMS builds on two established technologies: the Fast Integrated Mobility Spectrometer (Wang et al. 2017a, 2017b) and laminar flow water-based condensation methodology (Hering et al. 2014, Hering and Stolzenburg 2005). Inside WFIMS, particles of differing electrical mobility are separated in a drift tube and subsequently enlarged through water condensation. Particle size and concentration are measured via digital imaging at a frame rate of 10 Hz. By measuring particles of different mobilities simultaneously, the WFIMS resolves particle diameters ranging from 8 to 580 nm within 1 second or less.

The performance of WFIMS was characterized with Differential Mobility Analyzer (DMA) classified $(\text{NH}_4)_2\text{SO}_4$ particles with diameters ranging from 8 to 265 nm. The mean particle diameters measured by WFIMS were found to be in excellent agreement with DMA centroid diameters. Furthermore, detection efficiency of WFIMS was characterized using a condensation particle counter as a reference and is nearly 100% for particles with diameter greater than 8 nm. In general measured and simulated WFIMS mobility resolutions are in good agreement. However, some deviations are observed at low particle mobilities, likely due to the non-idealities of the WFIMS electric field.

1. Introduction

In the last decades the role of atmospheric aerosol particles in determining the earth's radiative budget, climate change and air quality has been recognized. In this context the characterization of spatial and temporal variations of particle number size distributions, especially in the nanometer size range, is essential. Real-time measurements of particle size distributions are often required to capture highly dynamic aerosol processes, such as atmospheric new particle formation. In addition, measurement of spatial and temporal variations of aerosols onboard fast-moving platforms, such as aircrafts, also requires high time resolution. Capture of aerosol dynamics occurring on very small time scales requires instrumentation that, *inter alia*, has high sizing-accuracy, a wide size range, high time resolution, and good counting statistics.

One of the most widely used instruments for particles below about 500 nm is scanning mobility particle sizer (SMPS). The SMPS sequentially measures particle number concentrations within a narrow size (mobility) range. To obtain entire particle size distributions, a SMPS scans over a wide range of classifying voltages. This yields high sizing accuracy in a wide size range. However, the scanning process typically takes a few minutes (Flagan 1999). Wang et al. (2002) reduced the scanning time to 1 - 2 seconds by using a fast-response detector. However, particularly in clean environments the scanning time remains limited by the time required to obtain statistically relevant data. Other instruments based on electrical mobility classification, such as the electrical aerosol spectrometer (Mirme 1994, Mirme et al. 1984, Tammet et al. 1998, 2002), the engine exhaust particle sizer (Johnson et al. 2004) and the differential mobility spectrometer (Biskos et al. 2005) achieve high time resolution by measuring different mobilities simultaneously using an array of integrated electrometers. However, the low sensitivity of those detectors limits measurements to highly concentrated aerosols, such as engine exhausts. The differential mobility analyzer train (DMA-train; Winkler et al. 2013) achieves high time resolution in the 3 to 10 nm size range by operating a set of DMAs in parallel. While this approach offers faster measurement speed at atmospheric relevant particle number concentrations, the size resolution, determined by the number of DMAs, is comparatively low.

A heptanol-based Fast Integrated Mobility Spectrometer (FIMS) with wide dynamic size range was recently developed (Wang et al. 2017a, 2017b). Covering the 8 to 600 nm particle diameter range in a single snapshot, FIMS provides high-resolution, 1-sec size distribution measurements. The heptanol FIMS consists of a drift channel to spatially separate particles of differing electrical mobility, a condensational growth channel and an optical particle detector. Heptanol vapor is introduced with the sheath flow in the separator. Mobility-separated particles are enlarged through condensational growth along their flow trajectories, and their positions within the channel are captured via digital imaging. Thus FIMS combines the precision of electrical mobility sizing with the speed and sensitivity of optical particle counting.

In this paper, we present the performance characterization of a new Water-based FIMS (WFIMS), which combines measurement speed and precision of the heptanol-based FIMS with the water-based condensation methodology (Hering et al. 2005; Hering and Stolzenburg 2005; Spielman et al. 2017). Using water, rather than heptanol, to grow particles for detection has several advantages. First, WFIMS allows measurements in environments where chemicals such as heptanol are prohibited (e.g. clean rooms). In WFIMS, the mobility separation can be

accomplished at a range of relative humidity (RH), allowing measurements of particle hygroscopicity when WFIMS is used in tandem with a DMA (Pinterich et al. 2017). Other practical advantages of using WFIMS rather than FIMS are that certification and transport of water-based instruments is much easier, and there are essentially no occupational health concerns related to their operation.

2. Instrument Design

Figure 1

The WFIMS consists of four main sections, namely: entrance, separator, growth channel and detector (see Fig. 1). As with its predecessor FIMS (Kulkarni and Wang 2006a, 2006b), a parallel plate geometry defines a rectangular flow channel with a cross-sectional area in the (x,y) -plane. In this study, we have adopted the same coordinate system used in Fig. 1 of Wang (2009), which differs from the one used in Kulkarni and Wang (2006a, 2006b). Particle free sheath air is first dried using a nafion drier (Perma Pure, PD-200T-24MSS) before it enters the channel through two opposing ports located at the top of the entrance section. Subsequently the sheath flow is evenly distributed using a laminarizing mesh. The aerosol flow enters the main channel through a narrow slit (0.03 cm x 12.7 cm) along the y -direction in the grounded electrode (left electrode in Fig. 1) of the separator. The gap of the channel is reduced from 1.12 cm as in the heptanol FIMS (Wang et al. 2017a) to 0.9 cm in order to eliminate the flow instability due to buoyancy generated by heating of the flow in the growth channel (see more details about the growth channel below). Hence WFIMS channel cross-section is now 0.9 cm x 12.7 cm and operates at 16.5 l/min of total flow (a detailed table listing key physical and operation parameters of WFIMS can be found in the online Supplemental Information, S.1). Constant total flow Q_{tot} through the channel is achieved by a vacuum pump along with a critical orifice (O'Keefe Controls Co., No. 55). The desired aerosol flow Q_a , measured with a laminar flow element (capillary tube with ID ~ 0.13 cm) and a differential pressure transducer (Omega, PX653-01D5V), is maintained via PID control of the sheath air flow Q_{sh} using a proportional solenoid control valve (MKS, 0248A). At standard operating conditions the flow ratio Q_a/Q_{sh} is set at about 0.02.

Figure 2

The same electrode as in the FIMS using heptanol as working fluid (Wang et al. 2017a) is employed here. The HV electrode is made of a PCB board, which is positioned in the (y,z) plane and consists of 61 straight copper traces running in z -direction (i.e., the direction of flow). The applied voltage increases exponentially with the y position of the trace from $V_1 = 20$ V at $y = -3$ cm to 1800 V, then linearly from 1800 to $V_2 = 6000$ V at $y = +3$ cm, such that the maximum voltage difference among adjacent traces is limited to 300 V to avoid arcing. Minimum and maximum voltages V_1 and V_2 are applied from $y = -6$ to -3 cm and from $+3$ to $+5$ cm, respectively. The spatially varying electric field generated by the HV electrode is simulated using COMSOL MultiphysicsTM, and presented in Fig. 2. Note the electric field is assumed to be independent of z -coordinate (the flow direction), and this assumption will be further discussed later. The spatially varying electric field provides two-dimensional size separation of aerosol

particles in the (x,y) -plane. At the exit of the separator, the positions of monodispersed particles form an arc in the cross section of the channel, i.e. (x,y) -plane, instead of a straight line in the FIMS employing a uniform electric field (Kulkarni and Wang 2006a). Forming an arc trajectory itself does not have any advantage over a straight line for monodispersed particles. An arc trajectory for monodispersed aerosol is a result of spatially varying electric field (i.e., the strength of electric field varies with y position), which is necessary to enhanced the dynamic size range of the WFIMS. Particles with higher mobility are distinguished at the bottom end ($y < 0$) of the channel and lower mobility particles at the top (see Fig. 2b and 4b). To avoid edge effects of the electric and flow fields particle detection is limited to $-3.5 \text{ cm} \leq y \leq +3.5 \text{ cm}$ (Fig. 4a).

Figure 3

After being positioned by the separator, particles enter a water-based condensational growth channel. In contrast to FIMS, the WFIMS introduces the vapor needed for particle condensational growth after the mobility separation, an option made more practically feasible by the high diffusivity of water vapor. Thus the relative humidity within the mobility separation region may be controlled independently. Typically WFIMS is operated with low humidity in the separator, thereby providing dry, mobility-based particle sizing. The growth channel has three stages (see Fig. 3a): a cold “conditioner”, to cool and humidify the aerosol; a warm “initiator” to introduce water vapor, leading to a supersaturation; and a cold “moderator”. The moderator technique is described in Hering et al. (2014), which shows that once the supersaturation is created by the warm, wet walls of the initiator section, the saturation profiles are fairly insensitive to a downstream decrease in the wall temperature, provided the walls are wet. The purpose of the moderator section is to lower the dew point so that the exiting air does not fog the camera window and other components, while allowing the supersaturation and growth to persist. The conditioner and moderator sections are operated below the temperature inside the separator, while the initiator is warmer. The smallest particle size that is activated to grow is primarily dependent on the maximum supersaturation inside the growth channel, which is largely controlled by the difference between the initiator and conditioner temperatures. The dew point of the flow exiting the growth channel depends mostly on the moderator temperature. Figure 3b shows contour plots of modeled water vapor saturation ratio (solid lines) and equilibrium Kelvin diameter (dashed lines), which we use to approximate the diameter of the smallest particle that can be activated, inside the growth channel. Vapor supersaturation is achieved in most of the initiator-moderator region, and peak saturation ratios higher than 1.4 occur in the central region just downstream of the initiator exit, at axial positions ranging from about 5 to 7 cm. The equilibrium Kelvin diameter in this region, which corresponds to the central 50% of the viewing window, is 5.5 nm and smaller. The contour line representing a Kelvin diameter of 7 nm indicates that particles down to that size could be activated within the entire viewing window.

To preserve the (x,y) positions of particles as they grow, flow obstructions within the growth channel were minimized by fabricating wicks from 0.6 cm thick sheets of alumina bisque, a porous partially-fired ceramic, one pair for each section of the growth channel. They form channel walls that are flat to within about 50 μm . Additionally the stiffness of the alumina allows the wicks to be held in place only by clamps at the edges of the channel. Each of the six wicks is clamped against an O-ring to create a thin, air-tight, water-filled reservoir against the aluminum housing. Water is drawn up into the reservoirs from a reservoir about 30 cm below the bottom of

the growth channel. The resulting negative pressure prevents water from dripping into the flow channel, without the need for a physical barrier. The wick surfaces are completely saturated; any excess water is quickly drawn inside the porous material, but surface tension prevents air from entering (Baker 2012). At the end of the growth channel, grown droplets are illuminated with a sheet laser beam (Coherent, Mag II, $\lambda = 680$ nm). The image of the illuminated droplets is captured using a focusing lens (Nikon, NIKKOR 50 mm) and a CCD camera (Dalsa, Pantera 1M60) operated with a frame rate of 10 Hz.

3. Image Processing and transfer function simulation

Particle sizes and number concentrations are determined by processing images acquired with the CCD camera. To this end positions of individual particles are derived from recorded camera frames using MATLAB's Image Processing Toolbox. Measured particle positions (see Fig. 4a) are then converted to instrument response mobilities Z_p^* through interpolation using a map of instrument response mobilities (see Fig. 4b) derived from simulated trajectories (Wang 2009, Wang et al. 2017a). Finally, instrument response mobilities are converted into instrument response diameters D_p^* assuming singly charged particles (see Fig. 4c).

Figure 4

Instrument response mobilities Z_p^* are mapped using the simulated positions at the separator exit for non-diffusing particles introduced along the central aerosol flow stream line. Note for non-diffusing particles, these positions are essentially the same as those detected following growth. The simulation of particle trajectories was carried out for particles of 2500 diameters evenly spaced on a logarithmic scale from 4 to 900 nm. Particles of each size were introduced into the separator at 1001 locations y_{in} evenly spaced from $y = -4.00$ cm to $+4.00$ cm along the central aerosol flow streamline. The velocity and trajectory of each particle inside the separator was calculated from the particle electrical mobility, the electric field, and the flow field. The flow field is assumed to be fully developed, with a parabolic profile and non-zero component only in the z -direction. WFIMS transfer functions are based on simulated trajectories of particles introduced along 101 aerosol flow streamlines evenly spaced between the boundaries of the aerosol flow, and at 1001 y positions along the width of the inlet. Brownian motion of particles was simulated using Monte Carlo techniques, and for particles introduced at several flow stream lines and y positions, the simulation was repeated 10 times (Wang et al. 2017a). These resulted in the simulation of about 10^6 trajectories for each particle size. The Brownian motion of particles was simulated beyond the separator, until the point of particle activation in the growth channel. Particle trajectories were actually calculated until 2.5 cm after the beginning of the initiator representing the upper limit for the impact of diffusion on particle positions. We assume that the contour line corresponding to a Kelvin equilibrium diameter of 7 nm in Fig. 3b represents the maximum distance L_a particles travel between the end of the electrode and the point of their activation. Within the viewing window this distance varies between 1 and 4 cm. Such a small uncertainty in L_a (± 1.5 cm) is expected to have a very minor impact on simulated particle positions and transfer functions (Wang et al. 2017b), hence we used the mean maximum distance, i.e. 2.5 cm, for our simulations. A more detailed description of particle trajectory simulations can be found elsewhere (Wang et al. 2017a).

As in the heptanol-based FIMS, only particles detected within the viewing window are used to derive particle sizes and concentrations, minimizing the impact of the edge effects of both flow and electric fields. The viewing window corresponds to a central region of $0.2 \cdot a \leq x_f \leq 0.8 \cdot a$, with $a = 0.9$ cm being the flow channel gap, and -3.5 cm $\leq y_f \leq +3.5$ cm (see Fig. 4a: viewing window highlighted in white). Additionally, experimentally determined effective voltages V_1^{eff} and V_2^{eff} are used to simulate the electric field and particle trajectories to account for instrument non-idealities. A detailed description of the procedure for determining the effective voltages is in the online Supplemental Information S.2.

4. Experimental Setup

Figure 5

The WFIMS was characterized using monodisperse ammonium sulfate $(\text{NH}_4)_2\text{SO}_4$ particles classified by a cylindrical DMA (TSI Inc., Model 3081/3085). WFIMS has a measurement size range of 8 to 580 nm (see Fig. 8), however we focused the experimental characterization on smaller sizes from 8 to 265 nm, because the size dependence of particle detection efficiency and the impact of Brownian diffusion on the instrument's resolution are more pronounced at small sizes. A schematic diagram of the experimental setup is shown in Fig. 5. Particles ranging from 8 nm to 100 nm in diameter were generated by atomizing a dilute $(\text{NH}_4)_2\text{SO}_4$ solution (0.75 mM) using a constant output atomizer (TSI Inc., Model 3076), followed by a diffusion dryer, a tube furnace operated at a temperature of 230 °C, and a heat exchanger. Larger particles with diameters ranging from 100 to 265 nm were generated by atomizing a dilute $(\text{NH}_4)_2\text{SO}_4$ solution (7.6 mM) followed by diffusion drying only. To achieve stable particle number concentrations ranging from 1 to 100 cm⁻³ the dilution of the output aerosol was optimized by adapting (i) the diameter of a limiting orifice in dilution stage 1 and/or (ii) the dilution flow via a needle valve (dilution stage 2). The diluted polydisperse particles were introduced into a ⁸⁵Kr bipolar aerosol neutralizer (TSI Inc., Model 3077) and subsequently classified in a DMA to obtain monodispersed particles. Particles smaller or equal to 50 nm were classified with a nano-DMA (TSI Inc., Model 3085), above 50 nm a long-column DMA (TSI Inc., Model 3081) was used. The ratio of DMA aerosol to sheath and sample to excess flow was kept constant at 1:10, while DMA sheath flow was switched between 8 l/min and 14.2 l/min to optimize the size range of classified particles and the resolution of the DMA. To maintain constant WFIMS and CPC (TSI Inc., Model 3010) inlet flows, Q_a and Q_{CPC} , respectively, a variable particle free makeup flow, Q_{Tr} , was mixed with the monodispersed aerosol flow exiting the DMA before introduced to WFIMS and CPC. Note to avoid any potential uncertainties introduced by particle charging efficiency we removed the aerosol neutralizer from WFIMS inlet in this study. The temperature difference between CPC condenser and saturator was increased to 21°C to increase the counting efficiency below 20 nm (Mertes et al. 1995). Size dependent CPC counting efficiencies η_{CPC} of positively charged ammonium sulfate particles at a CPC sample flow rate of 1.1 l/min were determined using an electrometer (TSI Inc., Model 3068B) as reference. The calibration yielded a CPC cutoff diameter, $D_{p,50}$, of 8 nm in agreement with the data presented in Mertes et al. (1995).

WFIMS aerosol and total flow, Q_a and Q_{tot} , were maintained at 0.3 l/min and 16.5 l/min, respectively. Differences between growth channel temperatures and the separator temperature ($\sim 25^\circ\text{C}$), ΔT_{con} , ΔT_{ini} and ΔT_{mod} were kept at -12°C , $+28^\circ\text{C}$ and -10°C , respectively. Minimum and maximum voltages V_1 and V_2 applied across the HV electrode were set to 20 V and 6000 V, respectively. Before starting each experiment, the aerosol generation system was allowed to stabilize and flows were calibrated with a flow calibrator (Gilian Instruments, Gilibrator).

5. Results and Discussion

The performance of the WFIMS, as characterized by its sizing accuracy, detection efficiency, and mobility resolution was evaluated using the experimental setup described above.

5.1 Size measurement with DMA classified aerosol

The sizing accuracy of WFIMS was assessed by comparing mean diameters measured by WFIMS with DMA centroid diameters for particles ranging from 8 to 265 nm. For each selected particle size CCD images were acquired over a period Δt of 10 minutes.

Figure 6

Figure 6 shows the instrument response diameter $D_{p,WFIMS}^*$, which is derived from instrument response mobility Z_p^* measured by WFIMS assuming singly charged particles. As can be seen from this graph DMA and WFIMS diameters are in good agreement indicating a high sizing accuracy of the latter. For the entire size range, i. e. 8 – 265 nm, the maximum deviation between $D_{p,WFIMS}^*$ and $D_{p,DMA}$ never exceeded 2%.

5.2 Counting Efficiency

Particle size and concentration dependent WFIMS counting efficiency η , i. e. the fraction of the particles within the viewing window that are detected by WFIMS, was evaluated by comparing total particle number concentrations measured by the WFIMS, i.e. N_{WFIMS} , to those measured by a CPC using

$$\eta = \frac{\eta_{CPC} \cdot N_{WFIMS}}{N_{CPC}} \quad (1)$$

with η_{CPC} being the CPC counting efficiency and N_{WFIMS} being

$$N_{WFIMS} = \frac{n_{\Delta t}}{\Delta t \cdot Q_a} \quad (2)$$

where $n_{\Delta t}$ is the total number of particles counted within the viewing window during measurement period Δt and Q_a is the aerosol sample flow rate.

In general the counting efficiency η of a particle counter is given by:

$$\eta = \eta_{\text{pen}} \cdot \eta_{\text{trans}} \cdot \eta_{\text{det}} \quad (3)$$

where η_{pen} , η_{trans} and η_{det} are penetration, transmission and detection efficiency, respectively. In the case of WFIMS the penetration efficiency η_{pen} describes particle losses along the inlet line, i.e. the flow passage between instrument inlet and mobility separator. WFIMS' transmission efficiency $\eta_{\text{trans}}(D_p)$ gives the fraction of particles entering the mobility separator that exit the growth channel within the viewing window. As the viewing window spans 7 cm in the center of channel cross section, only a fraction of particles introduced through the inlet slit, which spans the entire channel width of 12.7 cm, may be detected within the viewing window. This is accounted for in the transmission efficiency. Finally the detection efficiency η_{det} represents the fraction of particles exiting the growth channel within the viewing window that are detected by the CCD camera. Since the major modification to the heptanol-based FIMS with enhanced dynamic size range (Wang et al. 2017a, 2017b) is the replacement of the condenser with a three-stage water growth channel, following discussion will focus on η_{det} . A detailed description of penetration and transmission efficiencies is given in the online Supplemental Information S.3.

The detection efficiency η_{det} is given by

$$\eta_{\text{det}} = \frac{N_{\text{WFIMS}}}{N_{\text{CPC}}} \cdot \frac{\eta_{\text{CPC}}}{\eta_{\text{pen}} \cdot \eta_{\text{trans}}} \quad (4)$$

η_{det} mainly depends on whether particles grow to sufficient sizes to be detected optically, which is controlled by particle diameter and the local saturation ratio along the particle trajectories in the growth channel. Particle transport and growth inside the growth channel was simulated in a two-step process to estimate the lower size limit of WFIMS. First, the finite element modeling software package COMSOL Multiphysics[®] was used to determine the flow profile, temperature, and vapor concentration. The model also included the thermal conductivity of the wicks and the heat source/sink from condensation/evaporation at the surface. Then we used MATLAB to integrate the droplet growth along its trajectory in the supersaturated flow (Lewis and Hering 2013). The particle Brownian motion before activation inside the growth channel was neglected, and the trajectory of the particles was assumed to follow flow streamlines. From modeled water vapor saturation ratios and equilibrium Kelvin diameters inside the growth channel (see Fig. 3b), it can be concluded that particles as small as 5.5 nm can be activated and grow large enough ($>1 \mu\text{m}$) to be detected optically. In other words, no size dependence is expected for η_{det} .

Figure 7

As shown in Fig. 7a WFIMS' detection efficiency is essentially 100% for particles ranging from 8 to 265 nm in agreement with modeled water vapor saturation ratio and droplet growth described above. Deviations from unity, observed in both directions, are mostly within 10%, and could be due to the uncertainty in WFIMS and CPC measurements, at least partially. This also suggests that calculated transmission and penetration efficiencies capture actual particle losses and transport sufficiently well (see Eq. (4)). The data shown in Fig. 7a were measured at $N_{\text{CPC}} \leq 100 \text{ cm}^{-3}$. When the particle number concentration at a single particle size is significantly higher,

optical coincidences can lead to an underestimation of measured particle number concentrations. This measurement artefact is shown in Fig. 7b, where η_{det} is plotted as a function of N_{CPC} for DMA classified 100 nm ammonium sulfate particles. η_{det} decreases substantially as the number concentration of size-selected particles exceeds about 130 cm^{-3} , and at the concentration of 800 cm^{-3} , coincidence leads to a 30% underestimate of the concentration measured by the WFIMS. A way to correct for optical coincidences is shown in the online Supplemental Information section S.4. However, for the measurements of ambient aerosol particles, the upper concentration limit is much higher because WFIMS only measures charged particles and a fraction of the particles is lost during transport in the inlet line, especially for smaller particles. In addition, atmospheric aerosols are polydisperse. As a result, detected particles spread across the entire imaging window instead of a narrow “arc”, leading to negligible impact from coincidence at much higher total particle number concentrations. As shown in the online Supplemental Information section S.5, the impact of coincidence remains very minor ($< 1\%$) until the particle number size distribution exceeds those under typical polluted conditions by at least one order of magnitude, when particle charging efficiency and penetration efficiency are taken into consideration. Thus we expect that the impact of optical coincidence is largely negligible for measurements of ambient aerosol populations. It should be noted that it would be possible to increase the CCD frame rate from 10 to 60 Hz and thereby increase the upper concentration limit by a factor of about 6 if necessary, e.g. when sampling highly concentrated aerosol.

Figure 8

Given the essentially 100% detection efficiency, WFIMS’ counting efficiency η can be reduced to the product of penetration and transmission efficiency. The resulting size dependent counting efficiency shown in Fig. 8 exceeds 10% between 20 nm and 400 nm, exhibits a global maximum of about 21% at 140 nm and decreases to 1% and 5% at 10 nm and 580 nm, respectively. The non-monotonic behavior of $\eta(D_p)$ can be attributed to the shape of $\eta_{\text{trans}}(D_p)$ (see online Supplemental Information section S.3). A detailed analysis of WFIMS counting statistics shows that for typical remote continental aerosol (Jaenicke 1993), the relative uncertainty of 1 s WFIMS size distribution measurements is less than 30% for particles with diameters between 15 nm and 280 nm, a size range that dominates the overall particle number concentration (see online Supplemental Information section S.5). The uncertainties in total number concentration and mean particle diameter derived from 1-s measurements are about 6%.

5.3 Mobility Resolution

In addition to sizing accuracy and counting efficiency, mobility resolution of the WFIMS is evaluated by comparing its calculated and measured response to DMA classified particles ($D_{p,\text{DMA}} = 8$ to 265 nm). As an analytic form of WFIMS transfer function is not available, it is very challenging to characterize the WFIMS transfer function experimentally through fitting a few controlling parameters as was done in Kulkarni and Wang (2006b). Here we examine the WFIMS mobility resolution by comparing the shape of measured/simulated response mobility distribution $P^{\text{tot}}(Z_{p,\text{DMA}}, Z_p^*)$, where $Z_{p,\text{DMA}}$ and Z_p^* are DMA centroid diameter and WFIMS instrument response mobility, respectively. To facilitate the comparison, overall mobility resolutions $R_{\text{FWHM}}^{\text{tot}}$ and $R_{\text{std}}^{\text{tot}}$ are introduced. Note due to the unique shape of WFIMS’ transfer

function (Wang 2009, Wang et al., 2017a) $R_{\text{FWHM}}^{\text{tot}}$, the resolution based on FWHM, might fail to capture the overall spread of $P^{\text{tot}}(Z_{\text{p,DMA}}, Z_{\text{p}}^*)$ unlike $R_{\text{std}}^{\text{tot}}$, the resolution base on the standard deviation of $P^{\text{tot}}(Z_{\text{p,DMA}}, Z_{\text{p}}^*)$. A detailed derivation of $R_{\text{FWHM}}^{\text{tot}}$ and $R_{\text{std}}^{\text{tot}}$ can be found in the online Supplemental Information section S.6. In the following discussions, subscripts “std” and “FWHM” are omitted unless a clear distinction between R_{FWHM} and R_{std} is necessary.

Figure 9

As shown in Fig. 9, measured (open red diamonds) and simulated (solid red lines) overall mobility resolutions are in fairly good agreement. For DMA centroid diameters $D_{\text{p,DMA}}$ below 60 nm the mean deviation is about 6%. Between 60 and 250 nm simulated R^{tot} exceed measured ones by 15% on average. The cause of the discrepancy between 60 and 250 nm is studied by examining $P^{\text{tot}}(Z_{\text{p,DMA}}, Z_{\text{p}}^*)$ for particles detected in different sub-areas of the viewing window following the approach described in Wang et al. (2017b).

Figure 10

Figure 10a illustrates averaged measured (red) and simulated (green) particle positions at the growth channel exit for DMA classified ammonium sulfate particles ($D_{\text{p,DMA}} = 60$ nm). The red arc is rotated clockwise with respect to the green arc, which suggests that, for the same monodispersed aerosol, on average particles detected closer to the ground electrode ($x/a = 0$) were measured with a higher instrument response mobility Z_{p}^* than those detected near the HV electrode ($x/a = 1$). This shift in measured Z_{p}^* is further illustrated in Fig. 10b using normalized $P^{\text{tot}}(Z_{\text{p,DMA}}, Z_{\text{p}}^*)$ for different sub-areas of the viewing window. Blue, green and black lines correspond to detected particle x -positions x_{f} ranging from $0.2 \cdot a$ to $0.3 \cdot a$, $0.45 \cdot a$ to $0.55 \cdot a$ and $0.7 \cdot a$ to $0.8 \cdot a$, respectively. Clearly measured P^{tot} moves towards larger Z_{p}^* with increasing x_{f} limits. This results in a broader P^{tot} for the entire viewing window (red line) and hence lower mobility resolution R^{tot} than simulated (subplot (c)). The shift in measured P^{tot} towards larger Z_{p}^* with increasing x_{f} limits is likely due to non-idealities of the electric field, which are not represented by the simplified 2-D electric field used to simulate particle trajectories.

Better agreement between measured and simulated instrument resolution is found for narrower x_{f} ranges. This is demonstrated in Fig. 11, where R^{tot} for particles detected within $0.45 \cdot a - 0.55 \cdot a$ is plotted as a function of $D_{\text{p,DMA}}$. Note the narrower x_{f} range reduces the upper detectable size limit to 150 nm. Now measured R^{tot} , particularly $R_{\text{std}}^{\text{tot}}$, largely agree with simulations, while some minor discrepancies remain for particles larger than 40 nm. As the overall spread of $P^{\text{tot}}(Z_{\text{p,DMA}}, Z_{\text{p}}^*)$ is dominated by the width of DMA transfer function for particles larger than 40 nm (see Fig. 9), these minor discrepancies may be due to slightly degraded DMA resolution as reported in some of the earlier studies (e.g., Zhang and Flagan 1996). They attributed the degradation in the resolution of the cylindrical DMA and radial DMA partially to flow disturbance in the aerosol entrance slit. Similar flow disturbance near WFIMS aerosol inlet may lead to reduced R^{tot} , however, this impact seems to be minor given the better agreement in measured and calculated overall mobility resolutions for particles with diameters less than 40

nm. The better agreement between the size dependent R^{tot} for particles detected within sub-areas of the viewing window indicates that the Z_p^* shift in measured $P^{\text{tot}}(Z_{p,\text{DMA}}, Z_p^*)$ with varying x_f range is most likely the main cause for the discrepancy between measured and simulated overall mobility resolution corresponding to the entire viewing window for particles larger than 40 nm.

6. Conclusions

We present a Water-based Fast Integrated Mobility Spectrometer (WFIMS) with enhanced dynamic size range. The measuring principle is based on the Fast Integrated Mobility Spectrometer (Kulkarni and Wang 2006a, 2006b) with extended size range (Wang et al. 2009, 2017a and 2017b) and laminar flow water-based condensation methodology (Hering and Stolzenburg 2005). The WFIMS uses a drift channel to separate particles of differing electrical mobility. Subsequently the spatially separated particles are enlarged through water condensation along their flow trajectories, and their positions within the channel are captured via digital imaging. The growth channel is designed to use a “moderator” stage (Hering et al. 2014) to remove excess water vapor so as to provide the necessary condensational enlargement without risking condensation on the downstream optical components. Rather than sampling one size fraction at a time, as done with traditional mobility sizing systems, particles of different mobilities are detected simultaneously, with a data acquisition rate of 10 Hz.

WFIMS measures particles ranging from 8 to 580 nm in a single snapshot. However, we focused its performance characterization on DMA classified ammonium sulfate particles ranging from 8 to 265 nm in diameter, where the size dependence of detection efficiency and the impact of Brownian diffusion on transfer function were expected to be more pronounced. DMA centroid diameters agree well with particle sizes measured by WFIMS, indicating high sizing accuracy of the latter. Counting statistics analysis shows that the detection efficiency is nearly 100% for particles with diameters from 8 nm upwards. This is consistent with modeled saturation ratio profiles and droplet growth inside the growth channel. The WFIMS mobility resolutions are examined experimentally by studying the response of WFIMS to DMA classified monodispersed particles. The results indicate that for particles with diameters less than 40 nm, the WFIMS resolutions are well represented by the calculated resolutions based on simulated particle trajectories. For particles larger than 40 nm in diameter, degradation of WFIMS resolution is observed, and is likely due to non-idealities of the electric field, which yield variation in measured response mobility for particles detected with different x positions.

7. Acknowledgement

We thank Andrew McMahon, Scott Smith and Thomas Tsang for their help with the development of WFIMS. This work was supported by the U.S. Department of Energy's Small Business Innovation Research Program under contract DE-SC0013103, Small Business Technology Transfer Program under contract DE-SC0006312, and Atmospheric System Research Program (Office of Science, OBER) under contract DE-AC02-98CH10886.

References

- Baker, R. W. 2012. *Membrane Technology and Applications*. Wiley.
- Biskos, G., K. Reavell, and N. Collings. 2005. "Description and Theoretical Analysis of a Differential Mobility Spectrometer." *Aerosol Science and Technology* 39(6):527–41.
- Flagan, R. C. 1999. "On Differential Mobility Analyzer Resolution." *Aerosol Science and Technology* 30(6):556–70.
- Hering, S. V., S. R. Spielman, and G. S. Lewis. 2014. "Moderated Water Based Condensational Particle Growth in a Laminar Flow." *Aerosol Science and Technology* 48(4):401–8.
- Hering, S. V. and M. R. Stolzenburg. 2005. "A Method for Particle Size Amplification by Water Condensation in a Laminar Thermally Diffusive Flow." *Aerosol Science and Technology* 39(5):428–36.
- Hering, S. V., M. R. Stolzenburg, F. R. Quant, D. R. Oberreit, and P. B. Keady. 2005. "A Laminar Flow Water Based Condensation Particle Counter WCPC." *Aerosol Science and Technology* 39(7):659–72.
- Jaenicke, R. 1993. "Tropospheric Aerosols." *International Geophysics* 54:1–31.
- Johnson, T., R. Caldow, A. Pöcher, A. Mirme, and D. Kittelson. 2004. "A New Electrical Mobility Particle Sizer Spectrometer for Engine Exhaust Particle Measurements." *SAE 2004 World Congress & Exhibition* 2004-01–134.
- Kulkarni, P. and J. Wang. 2006a. "New Fast Integrated Mobility Spectrometer for Real-Time Measurement of Aerosol Size distribution—I: Concept and Theory." *Journal of Aerosol Science* 37:1303–25.
- Kulkarni, P. and J. Wang. 2006b. "New Fast Integrated Mobility Spectrometer for Real-Time Measurement of Aerosol Size Distribution: II. Design, Calibration, and Performance Characterization." *Journal of Aerosol Science* 37:1326–39.
- Lewis, G. S. and S. V. Hering. 2013. "Minimizing Concentration Effects in Water-Based, Laminar-Flow Condensation Particle Counters." *Aerosol Science and Technology* 47(6):645–54.
- Mertes, S., F. Schröder, and A. Wiedensohler. 1995. "The Particle Detection Efficiency Curve of the TSI 3010 CPC as a Function of the Temperature Difference between Saturator and Condenser." *Aerosol Science and Technology* 23(2):257–61.
- Mirme, A. et al. 1984. "Multi-Channel electric aerosol spectrometer." Pp. 155–159 in *11th International conference on atmospheric aerosols, condensation and ice nuclei*. Budapest, Hungary.
- Mirme, A. 1994. "Electrical Aerosol Spectrometry." UniversitatisTartuenssis,Tartu,Estonia.
- Pinterich, T., S. R. Spielman, S. V. Hering, and J. Wang. 2017. "A Humidity-Controlled Fast Integrated Mobility Spectrometer (HFIMS) for Rapid Measurements of Particle Hygroscopic Growth." *in preparation*.
- Spielman, S. R., S. V. Hering, C. Kuang, and J. Wang. 2017. "Preliminary Investigation of a Water-Based Method for Fast Integrating Mobility Spectrometry." *Aerosol Science and Technology* submitted.
- Tammet, H., A. Mirme, and E. Tamm. 1998. "Electrical Aerosol Spectrometer of Tartu University." *Journal of Aerosol Science* 29:S427–428.
- Tammet, H., A. Mirme, and E. Tamm. 2002. "Electrical Aerosol Spectrometer of Tartu University." *Atmospheric Research* 62:315–24.
- Wang, J., M. Pikridas, S. Spielman, and T. Pinterich. 2017a. "A Fast Integrated Mobility

- Spectrometer with Enhanced Dynamic Size Range, Part I: Design and Model Evaluation.” *Atmos. Meas. Tech.* 108.:44–55.
- Wang, J., M. Pikridas, T. Pinterich, et al. 2017b. “A Fast Integrated Mobility Spectrometer with Enhanced Dynamic Size Range, Part II: Experimental Characterization.” *Journal of Aerosol Science* accepted.
- Wang, J., V. F. McNeill, D. R. Collins, and R. C. Flagan. 2002. “Fast Mixing Condensation Nucleus Counter: Application to Rapid Scanning Differential Mobility Analyzer Measurements.” *Aerosol Science and Technology* 36:678–89.
- Winkler, P. M., J. Ortega, T. Karl, Peter H. McMurry, and James N. Smith. 2013. “A Fast-Scanning DMA Train for Precision Quantification of Early Nanoparticle Growth.” *AIP Conference Proceedings* 1527:165–68.

Figure 1 Schematic diagram of the Water-based Fast Integrated Mobility Spectrometer (WFIMS) (side view: (x,z) –plane, the y -axis is pointing out of the paper)

Figure 2 Electric field vectors (a) and equipotential lines (b) between separator electrodes. Both the length and the color of the field vector scale with the logarithm of the electric field strength. The gap a between separator electrodes is 0.9 cm (bottom view: (x,y) -plane)

Figure 3 (a) Temperature profile inside the growth channel showing flow stream lines (white) and relative humidity contours (black). (b) Contour plot showing modeled water vapor saturation ratio (solid lines) and equilibrium Kelvin diameter (dashed lines) inside the growth channel. The (warm) initiator extends from 0 to 5.1 cm. The laser position is 12.4 cm. (side view: (x,z) -plane).

Figure 4 (a) CCD image of DMA classified $(\text{NH}_4)_2\text{SO}_4$ particles ($D_p = 80$ nm). The white rectangle indicates the viewing window. (b) and (c) show maps of instrument response mobilities Z_p^* and corresponding instrument response diameter D_p^* of singly charge particles at the exit of the separator, respectively. (b) and (c) are based on particle trajectory simulations.

Figure 5 Experimental setup for characterizing the WFIMS.

Figure 6 Comparison of the mean diameter measured by WFIMS, $D_{p,\text{WFIMS}}^*$, and DMA centroid diameter, $D_{p,\text{DMA}}$.

Figure 7 WFIMS detection efficiency η_{det} as function of (a) particle diameter D_p for particle concentration $N_{\text{CPC}} < 100 \text{ cm}^{-3}$ and (b) particle number concentration N_{CPC} for particle diameter $D_p = 100$ nm. The area highlighted in yellow represents the $\pm 10\%$ uncertainty interval typical for particle counters.

Figure 8 WFIMS counting efficiency η as a function of particle diameter D_p .

Figure 9 Measured (open red diamonds) and simulated (solid red lines) overall mobility resolutions (a) $R_{\text{FWHM}}^{\text{tot}}$ and (b) $R_{\text{std}}^{\text{tot}}$ as a function of DMA centroid diameter $D_{\text{p,DMA}}$. Solid and dashed black lines indicate simulated WFIMS and DMA instrument mobility resolutions R_{WFIMS} and R_{DMA} , respectively.

Figure 10 (a) CCD image showing averaged simulated (green line) and measured (red line) positions of 60 nm ammonium sulfate particles at the separator exit. Corresponding normalized distributions P^{tot} derived from measured and simulated particle positions are illustrated in subplot (b) and (c), respectively. Line colors represent different viewing window sub-areas.

Figure 11 Measured (open diamonds) and simulated (solid line) overall resolution (a) $R_{\text{FWHM}}^{\text{tot}}$ and (b) $R_{\text{std}}^{\text{tot}}$ as a function of DMA centroid diameter $D_{\text{p,DMA}}$. The detection x -range is restricted to $0.45 \cdot a - 0.55 \cdot a$.

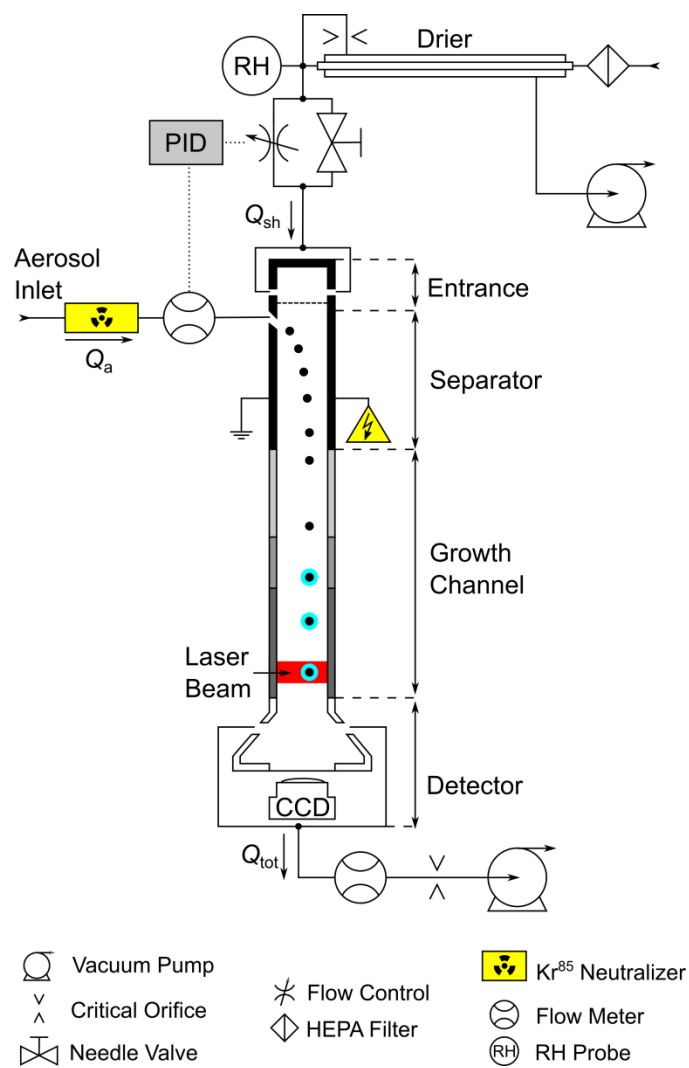


Figure 1

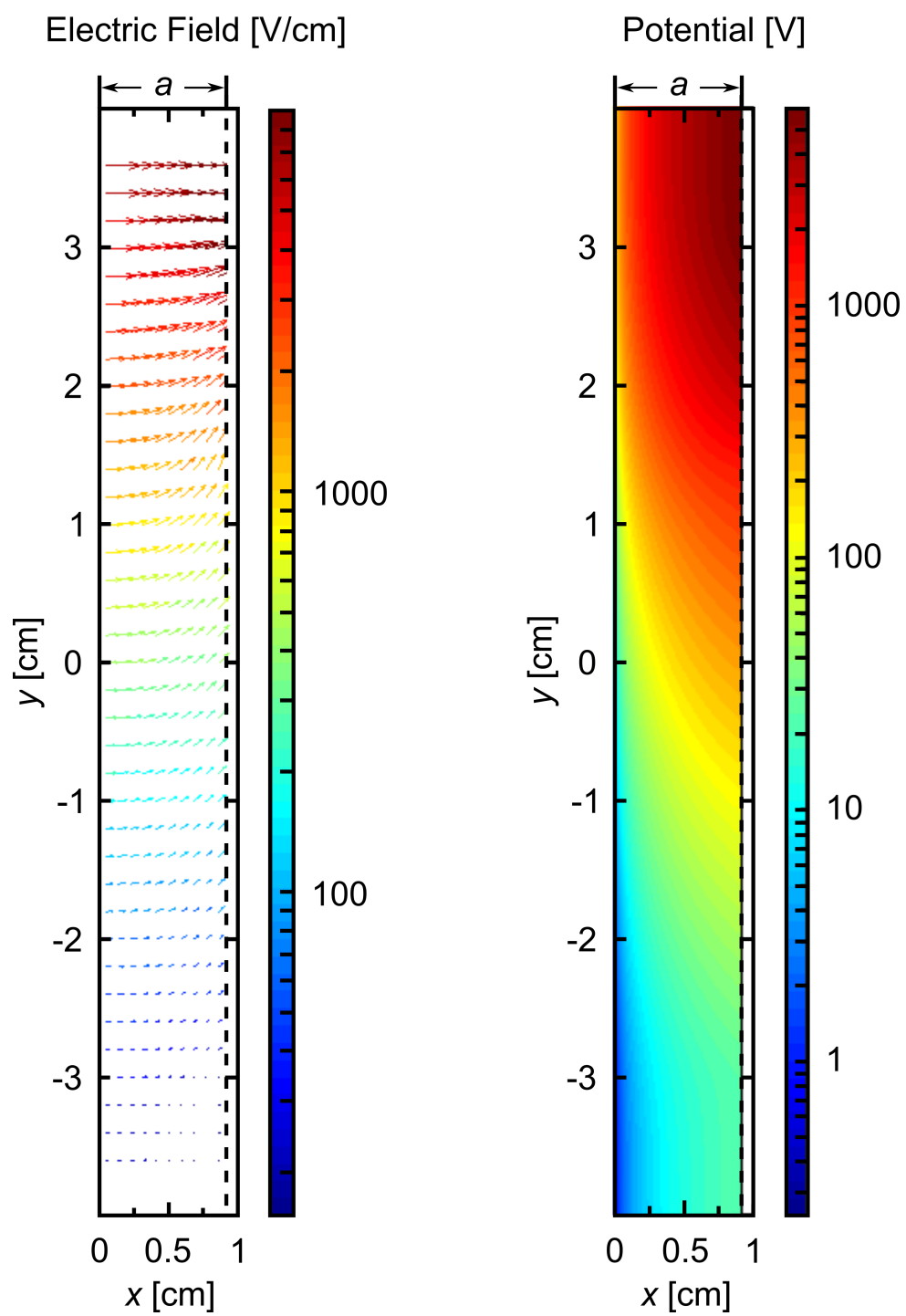


Figure 2

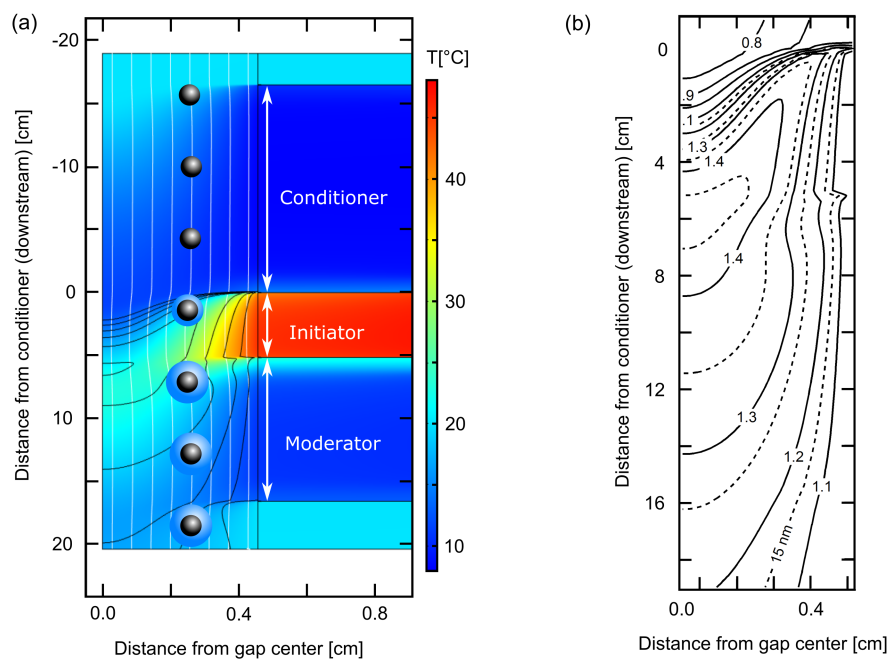


Figure 3

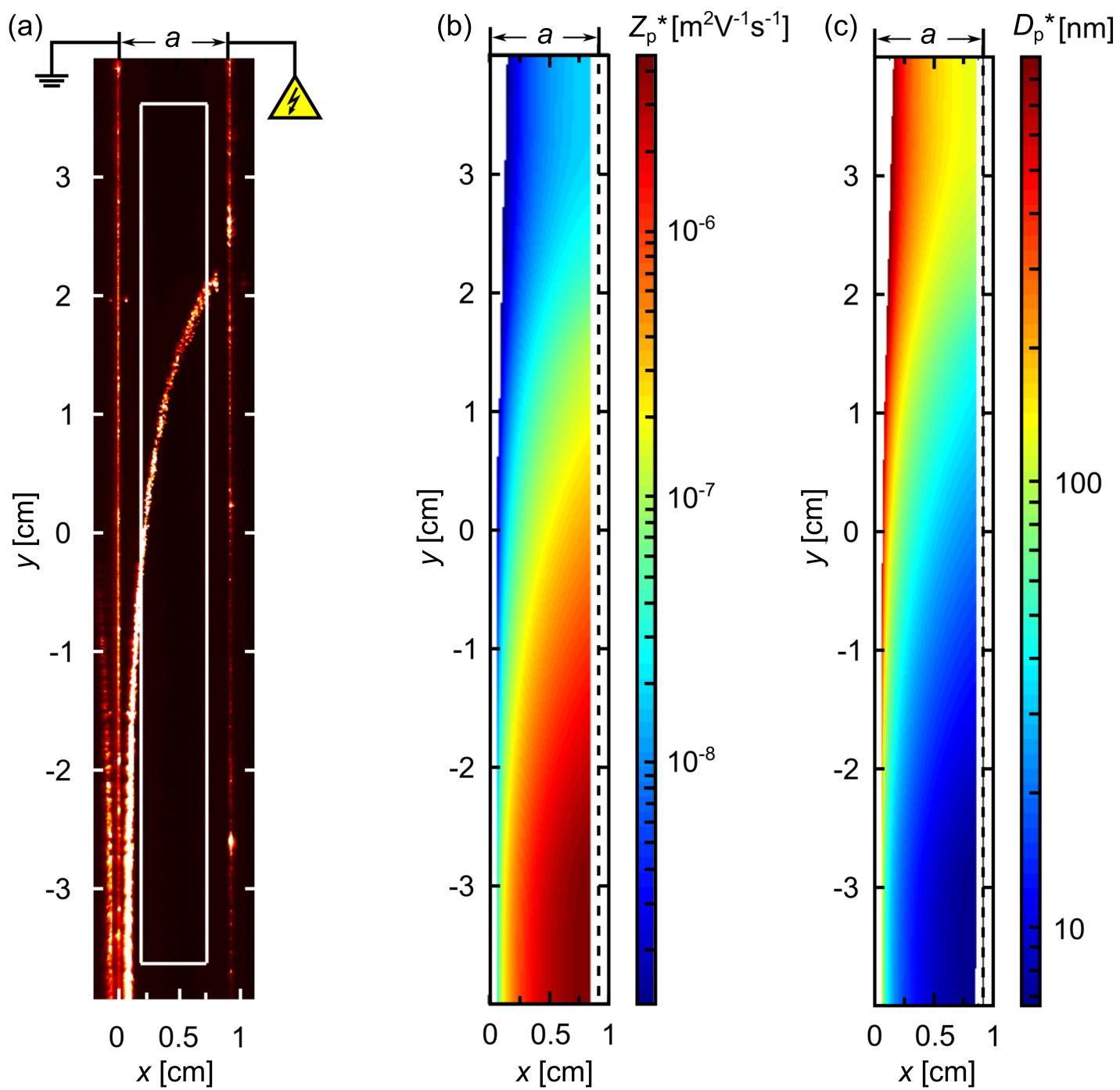


Figure 4

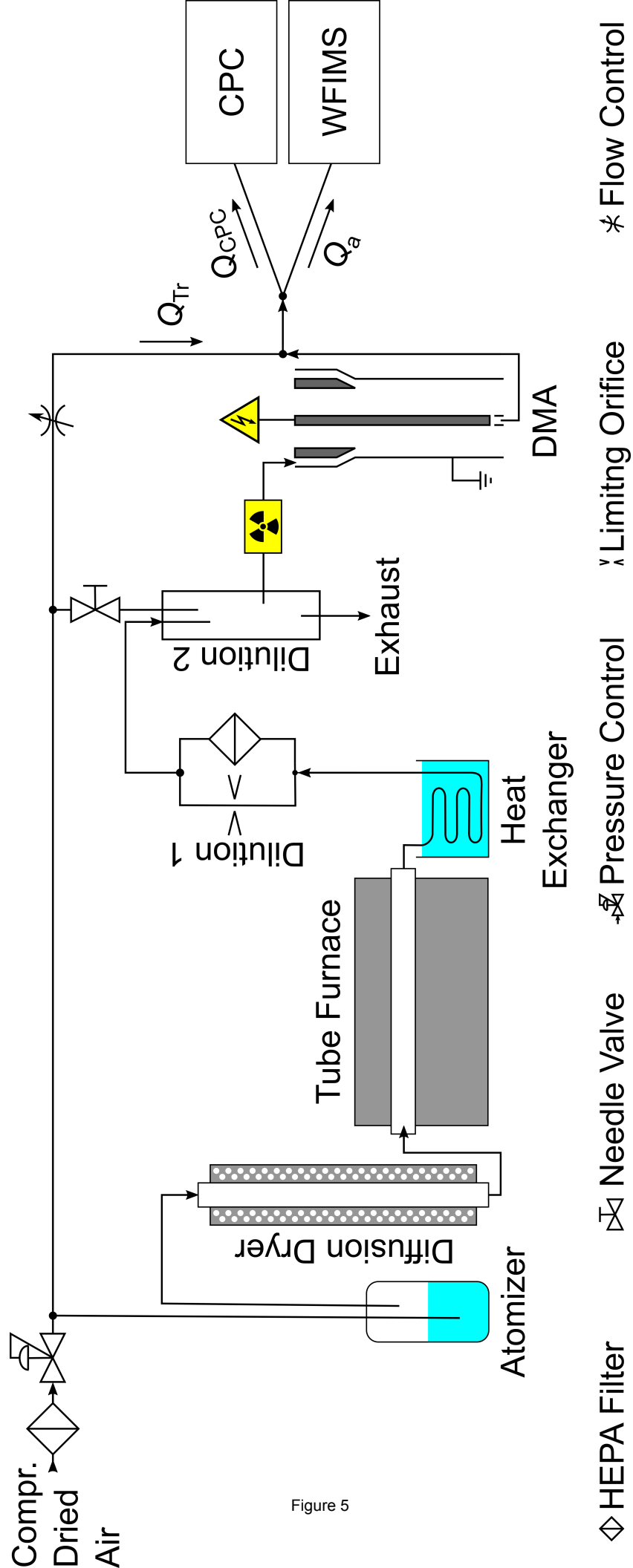


Figure 5

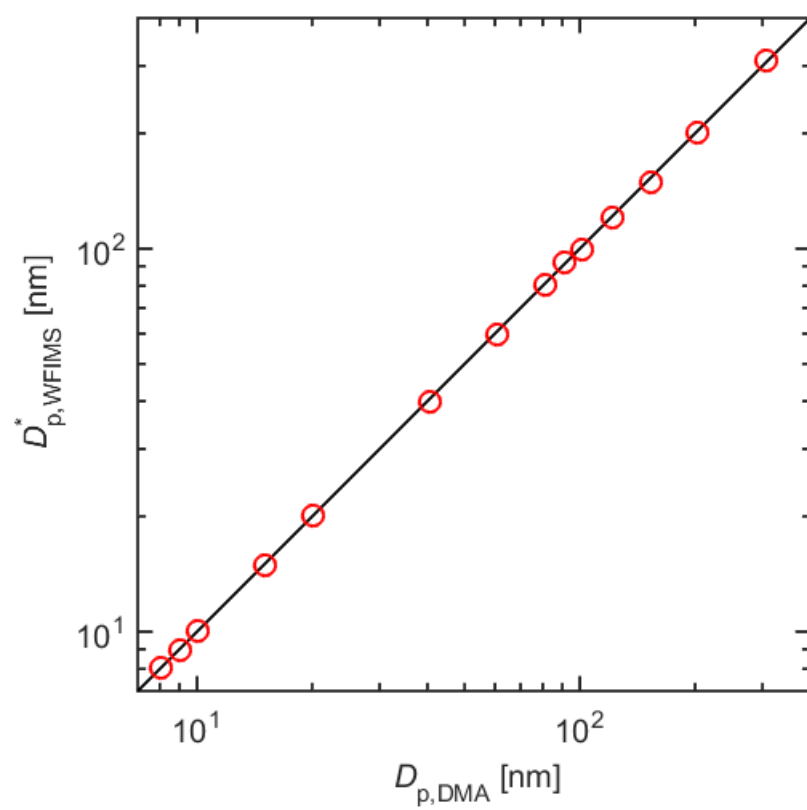
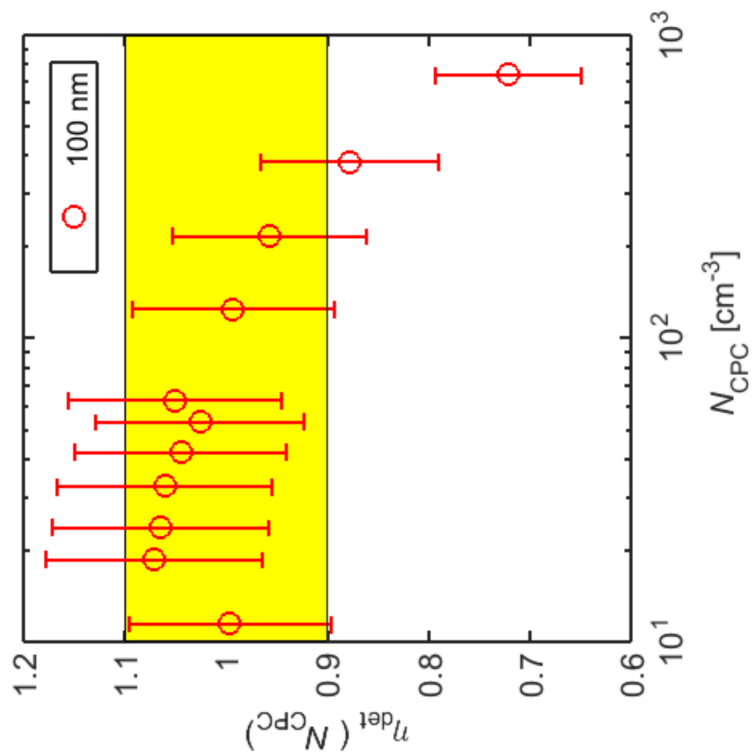
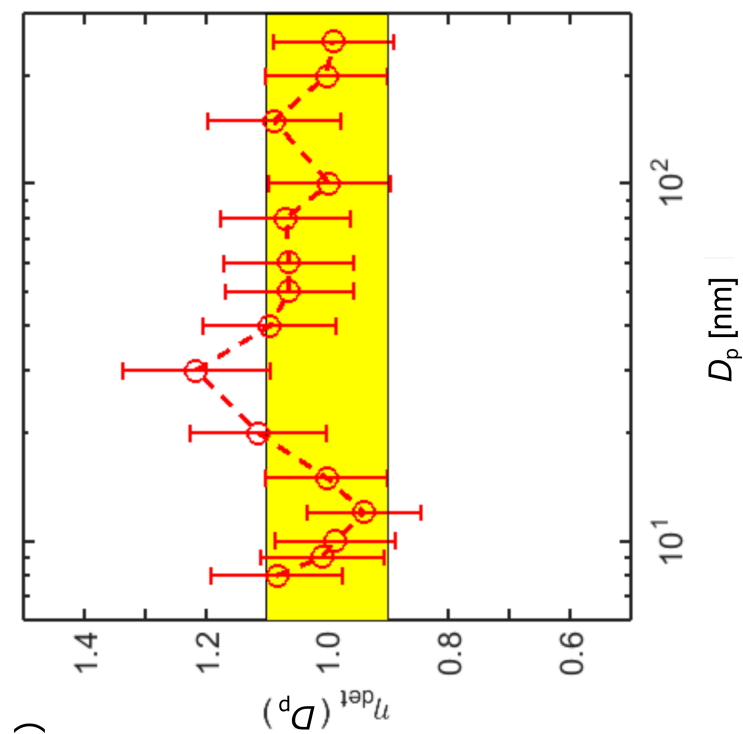


Figure 6



(b)



(a)

Figure 7

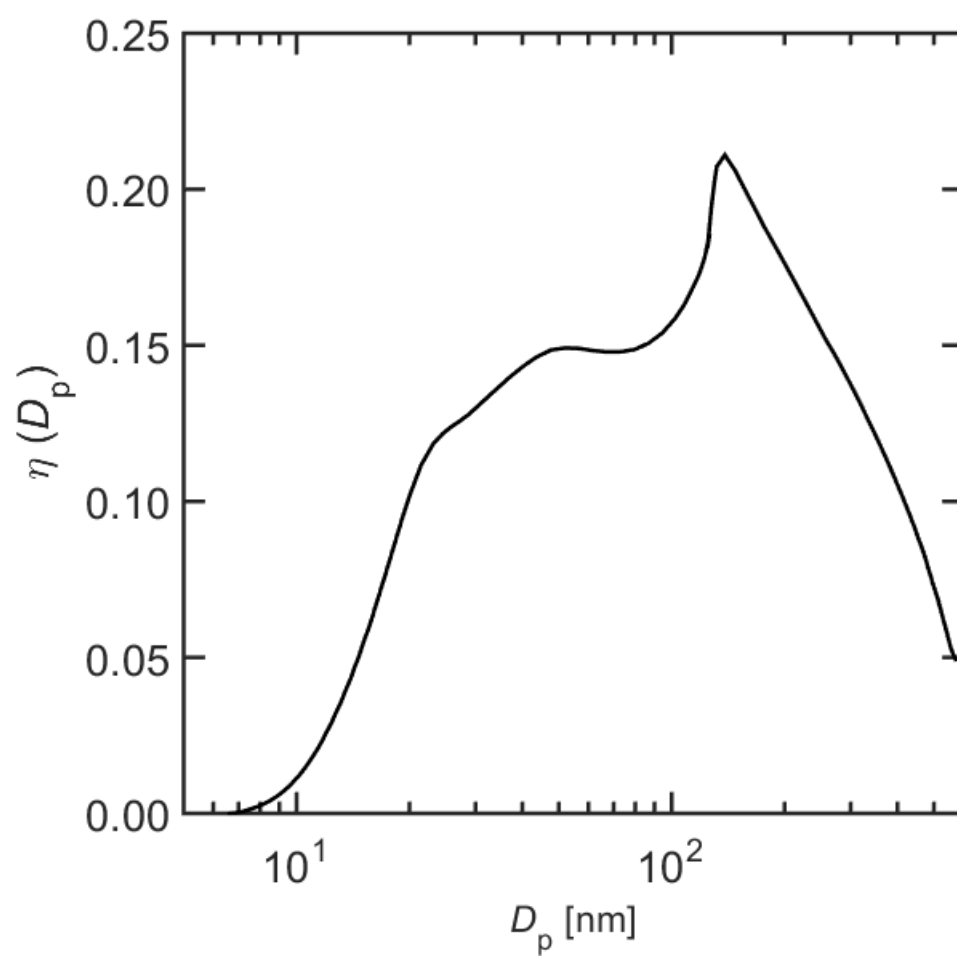


Figure 8

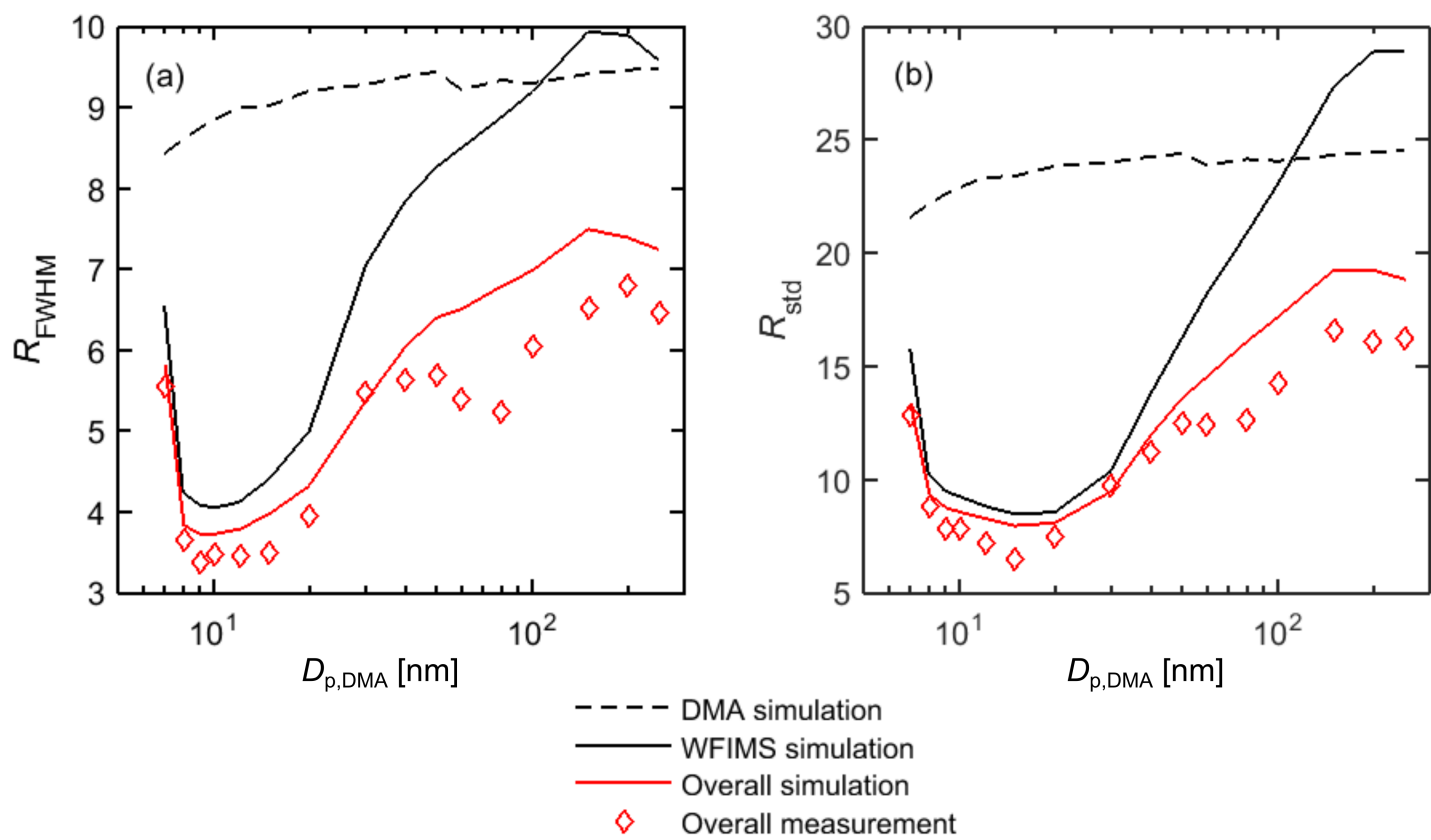


Figure 9

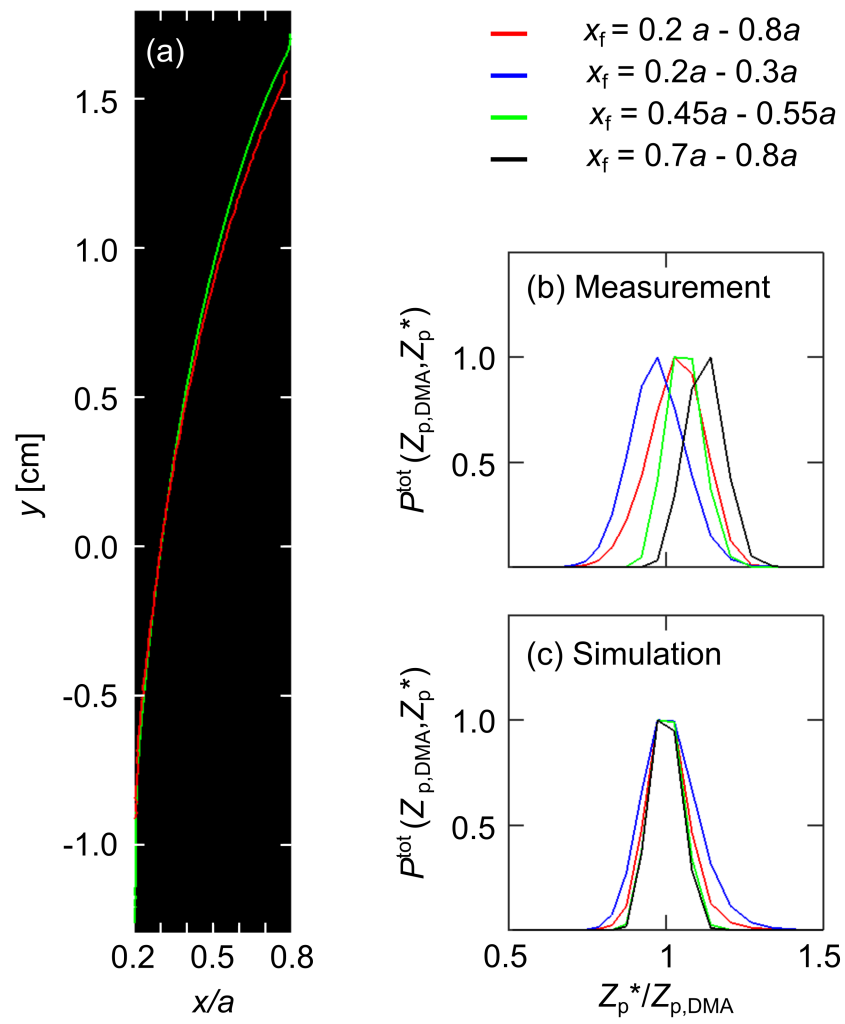


Figure 10

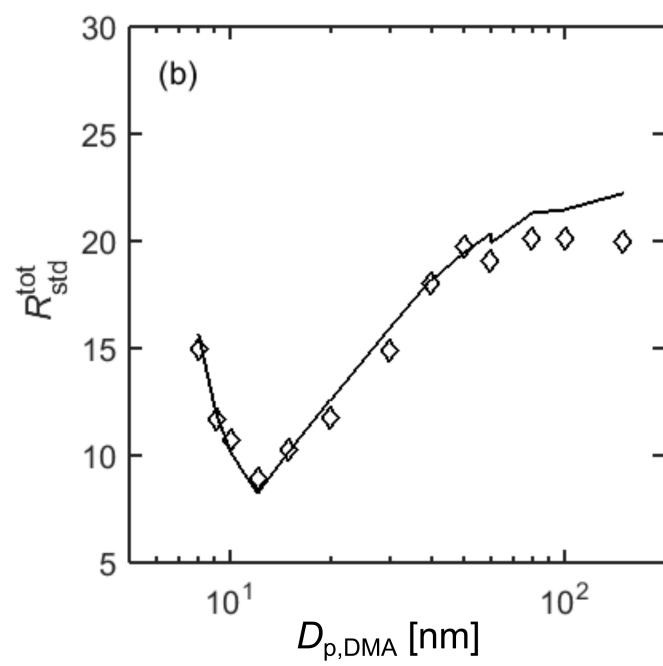
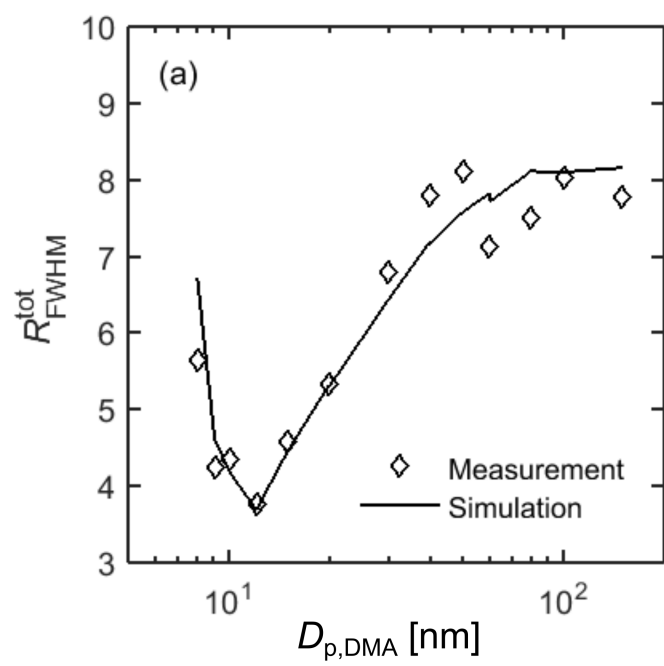


Figure 11

SUPPLEMENTAL INFORMATION

A Water-based Fast Integrated Mobility Spectrometer (WFIMS) with enhanced dynamic size range

Tamara Pinterich¹, Steven R. Spielman², Susanne V. Hering² and
Jian Wang^{1,*}

¹ Brookhaven National Laboratory, Upton, NY-11973-5000, USA

² Aerosol Dynamics Inc., Berkeley, CA-94710, USA

*Corresponding author mail: jian@bnl.gov

S.1 Key physical dimensions and operating parameters of WFIMS

Q_a	Aerosol flow	0.3 l/min
Q_{sh}	Sheath flow	16.5 l/min
V_1	Maximum voltage applied	6000 V
V_1^{eff}	Effective maximum voltage	6095 V
V_2	Minimum voltage applied	20 V
V_2^{eff}	Effective minimum voltage	24 V
ΔT_{con}	Conditioner	-12°C
ΔT_{ini}	Initiator	$+28^\circ\text{C}$
ΔT_{mod}	Moderator	-10°C
a	Distance between separator electrodes	0.9 cm
b	Width of flow channel = Entrance slit width	12.7 cm
	Entrance slit gap	0.0254 cm
L_{con}	Conditioner length	16.51 cm
L_{ini}	Initiator length	5.08 cm
L_{mod}	Moderator length	11.43 cm
x_{view}	Range in x -direction of viewing window	0.18 cm to 0.73 cm
y_{view}	Range in y -direction of viewing window	-3.50 cm to +3.50 cm

S.2 Calibration of the electric field

The electric field was calibrated with DMA classified particles using the following approach. First the effective maximum voltage was obtained with particles of low electrical mobility ($D_p > 100$ nm). Measured particle positions were converted into particle diameters (D_p^*) based on electric field and particle trajectories simulated using three different maximum voltages V_2^i :

$$\begin{aligned} V_2^1 &= 6000 \text{ V} \\ V_2^2 &= 6200 \text{ V} \\ V_2^3 &= 6400 \text{ V} \end{aligned}$$

together with the set minimum voltage V_1 of 20 V. This yielded three different average measured particle diameters $D_{p,\text{WFIMS}}(V_2^i, D_{p,\text{DMA}}^j)$ for each DMA selected particle size $D_{p,\text{DMA}}^j$.

$[V_2^i, D_{p,\text{WFIMS}}(V_2^i, D_{p,\text{DMA}}^j)]$ pairs were first fitted linearly:

$$D_{p,\text{WFIMS}}(V_2^i, D_{p,\text{DMA}}^j) = a^j \cdot V_2^i + b^j, \quad (\text{S.1})$$

with $i = 1, 2, 3$ and $j = \text{const.}$, to obtain $a^j = a(D_{p,\text{DMA}}^j)$ and $b^j = b(D_{p,\text{DMA}}^j)$. Then we fitted $D_{p,\text{DMA}}^j$ and parameters a^j and b^j to obtain effective voltage V_2^{eff} using least squares approach:

$$V_2^{\text{eff}} = \frac{\sum_j [(D_{p,\text{DMA}}^j - b^j) \cdot a^j / (D_{p,\text{DMA}}^j)^2]}{\sum_j (a^j / D_{p,\text{DMA}}^j)^2} \quad (\text{S.2})$$

An effective maximum voltage of 6095 V was obtained.

Then the effective minimum voltage was characterized using particles of high electrical mobility ($D_p < 20$ nm). This time the effective maximum voltage $V_2^{\text{eff}} = 6095$ V and three different minimum voltages V_1^i :

$$\begin{aligned} V_1^1 &= 16 \text{ V} \\ V_1^2 &= 20 \text{ V} \\ V_1^3 &= 24 \text{ V} \end{aligned}$$

were used to convert measured particle positions into particle diameters $D_{p,\text{WFIMS}}(V_1^i, D_{p,\text{DMA}}^j)$. Replacing V_2^i by V_1^i in Eq. S.1 the three data pairs $[V_1^i, D_{p,\text{WFIMS}}(V_1^i, D_{p,\text{DMA}}^j)]$ obtained for each particle size $D_{p,\text{DMA}}^j$ were fitted linearly to get fitting parameters a^j and

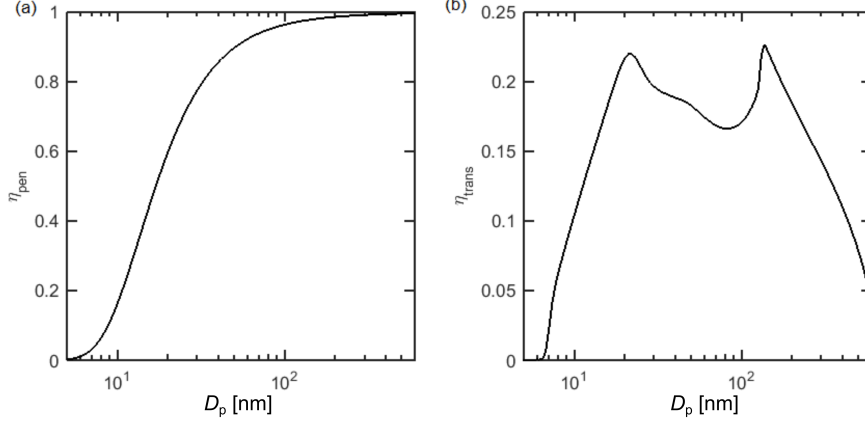


Figure S.1: Calculated penetration and transmission efficiencies, η_{pen} and η_{trans} , as a function of particle diameter D_p .

b^j . Then the effective low voltage V_1^{eff} was calculated using Eq. S.2. In the present study V_1^{eff} is 24.2 V.

S.3 WFIMS penetration and transmission efficiencies

Penetration losses along WFIMS inlet, which basically consists of a series of tubing and narrow rectangular flow channels, including the aerosol inlet slit in the ground electrode, were determined semi-empirically. First we used experimentally determined particle losses inside the removable inlet section connecting WFIMS front panel inlet and the inlet of the mobility separator to express penetration losses along this section in terms of Eq. 59 from Zhang and Flagan [9] using effective tubing lengths. Then we calculated particle losses in the mobility separator entrance slit based on Eq. 10 from Lee and Gieseke [4] using physical dimensions of the entrance slit. The resulting size dependent penetration efficiency is shown in Fig. S.1a.

WFIMS transmission efficiency $\eta_{\text{trans}}(D_p)$ is determined numerically based on particle trajectory simulations described earlier. The size dependent transmission efficiency η_{trans} is shown in Fig. S.1b. Between 13 and 265 nm η_{trans} exceeds 15%, has two maxima of about 22% at 22 and 138 nm and a local minimum of about 16.5% at 85

nm. Below and above that size range η_{trans} decreases to about 6% at 8 nm and 580 nm, respectively. This variation of $\eta_{\text{trans}}(D_p)$ is due to the combination of spatially varying electric field between the separator plates and the limits of the viewing window [6].

S.4 Optical coincidence

The effect of the optical coincidence on number concentrations measured by WFIMS is analyzed using experimental data obtained with 100 nm particles. The real particle concentration entering WFIMS is assumed to be N_{CPC} , the number concentration measured with a CPC running in parallel to WFIMS. Furthermore we assume that particles are distributed randomly within detection area A_{det} with an average particle density of n_c (see Fig. S.2a). Thus the probability of finding a nearest neighbor particle at any distance r between 0 and r from the reference particle is given by the integral of the 2-dimensional Hertz solution of Poisson distributed points at area concentration n_c

$$P(r) = 1 - \exp(-r^2 \pi n_c). \quad (\text{S.3})$$

The area density n_c reads

$$n_c = \frac{\eta \cdot N_{\text{CPC}} \cdot Q_a \cdot t_{\text{frame}}}{A_{\text{frame}}} \quad (\text{S.4})$$

with Q_a being the aerosol flow rate (0.3 l/min). t_{frame} is the time a frame is recorded (≈ 0.1 s) and $\eta(D_p)$ the size dependent counting efficiency (≈ 0.16 at 100 nm, see section 5.2).

If all nearest neighbors at distances $r' \in [0, r]$ from the reference particle cause optical coincidences, $P(r)$ is the probability of optical coincidences occurring during particle detection. Thus the number concentration N_{CPC} entering WFIMS is reduced by $N_{\text{CPC}} \cdot P(r)$ during optical detection and reads

$$\tilde{N}_{\text{WFIMS}} = N_{\text{CPC}} \cdot [1 - P(r)] = N_{\text{CPC}} \cdot \exp(-r^2 \pi n_c). \quad (\text{S.5})$$

Note \tilde{N}_{WFIMS} is the counting loss corrected number concentration measured by WFIMS ($\tilde{N}_{\text{WFIMS}} = N_{\text{WFIMS}} / \eta(D_p)$).

Ideally the image of each particle can be reduced to one maximum

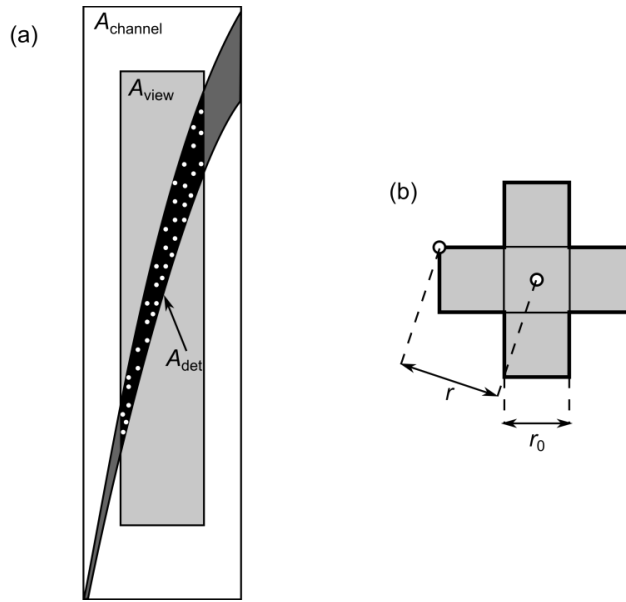


Figure S.2: Schematic diagram showing (a) Channel cross section A_{channel} , viewing window A_{view} and the area in which monodispersed particles are actually detected A_{det} . (b) Assuming particle spots can be reduced to 1 pixel the grey shaded area around a reference particle (located at the center) represents the coincidence region. r_0 is the length of a pixel, r indicates the distance between reference particle and its nearest neighbor.

intensity pixel. Then all particles falling within the grey shaded 5 pixel area shown in Fig. S.2b will cause optical coincidence with a reference particle positioned at the center of that area (center of the center pixel). The maximum distance r between two coinciding particles is given by the distance between any point on the circumference of the five pixel area (bold black line) and its center, and the average value is $1.22 \cdot r_0$ with r_0 being the width of a pixel (≈ 0.0074 cm). Based on experimentally determined particle positions A_{det} was found to be about 7.7% of the actual viewing window A_{view} , which is about 44% of the channel cross section A_{channel} ($0.9 \text{ cm} \times 12.7 \text{ cm}$).

To account for varying area density n_c across A_{det} and effective areas $r^2\pi$ deviating from $(1.22 \cdot r_0)^2 \pi$, we introduced an empirical correction factor k into the exponent of Eq. S.5 and fitted the function $f(N_{\text{CPC}}, k) = N_{\text{CPC}} \cdot \exp[-k \cdot r^2 \cdot \pi \cdot n_c(N_{\text{CPC}})]$ to \tilde{N}_{CPC} . In case of 100 nm particles k was found to be 7.9. Now summarizing all constants into one variable α

$$\alpha = -\frac{k \cdot (1.22 \cdot r_0)^2 \cdot \pi \cdot Q_a \cdot t_{\text{frame}} \cdot \eta}{A_{\text{det}}} \quad (\text{S.6})$$

\tilde{N}_{CPC} can be corrected using a Lambert W function [1] according to

$$\tilde{N}_{\text{CPC}}^{\text{corr}}(\tilde{N}_{\text{WFIMS}}) = \frac{W(\alpha \cdot \tilde{N}_{\text{WFIMS}})}{\alpha} \quad (\text{S.7})$$

Measured and corrected WFIMS number concentration plotted against N_{CPC} are presented in Fig. S.3.

S.5 Modeled size distributions detectable by WFIMS

To estimate the upper limit of aerosol size distribution that could be measured by WFIMS with negligible coincidence, we divided its detectable size range into n logarithmically spaced size bins having geometric mean bin diameters $\bar{D}_{p,i}$ and bin width $\Delta D_{p,i} \approx \bar{D}_{p,i}/20$, which is the typical size resolution of DMA. Taking into account that (i) WFIMS detects charged particles only, and (ii) some particles are lost during transport inside the inlet, we calculated the highest

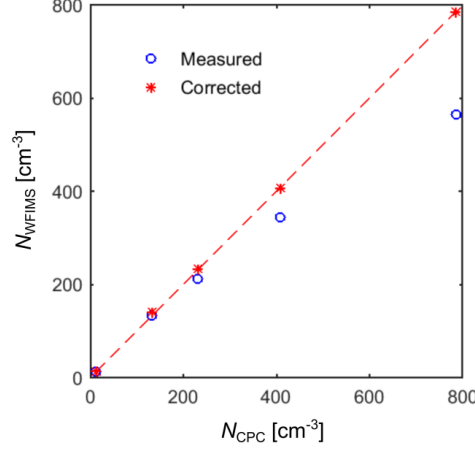


Figure S.3: Measured and coincidence corrected WFIMS number concentrations as a function of CPC number concentrations N_{CPC} . The dashed red line represents 1:1 correspondence.

number concentration detectable by WFIMS per size bin, i. e. $N_{\text{tot}}^{\text{max}}$, according to

$$N_{\text{tot}}^{\text{max}}(\bar{D}_{\text{p},i}) = \frac{N_{\text{eff}}}{\eta_{\text{pen}}(\bar{D}_{\text{p},i} \cdot f(+1, \bar{D}_{\text{p},i}))} \quad (\text{S.8})$$

where N_{eff} represents the maximum concentration of charged particles that survive the WFIMS inlet. Assuming N_{eff} is independent of particles size, it can be calculated as $130 \text{ cm}^{-3} \cdot \eta_{\text{pen}}(100 \text{ nm})$, where 130 cm^{-3} is the concentration limit at 100 nm, under which the impact of coincidence is negligible (less than 1%). $f(+1, \bar{D}_{\text{p},i})$ is the charging probability for singly, positively charged particles according to Wiedensohler [8].

Knowing $N_{\text{tot}}^{\text{max}}$ the maximum detectable particle number distribution $n_{\text{WFIMS}}(\log D_{\text{p}})$ can be approximated by

$$\begin{aligned} n_{\text{WFIMS}}(\log D_{\text{p}}) &= \frac{dN}{d\log D_{\text{p}}} \approx \frac{N_i}{\Delta \log D_{\text{p},i}} = \\ &= N_{\text{tot}}^{\text{max}}(\bar{D}_{\text{p},i}) / \log \left(\frac{D_{\text{p},i}^{\text{max}}}{D_{\text{p},i}^{\text{min}}} \right) \end{aligned} \quad (\text{S.9})$$

with $D_{\text{p},i}^{\text{max}}$ and $D_{\text{p},i}^{\text{min}}$ being upper and lower limit of size bin i . Figure S.4 shows $n_{\text{WFIMS}}(\log D_{\text{p}})$ together with particle number size

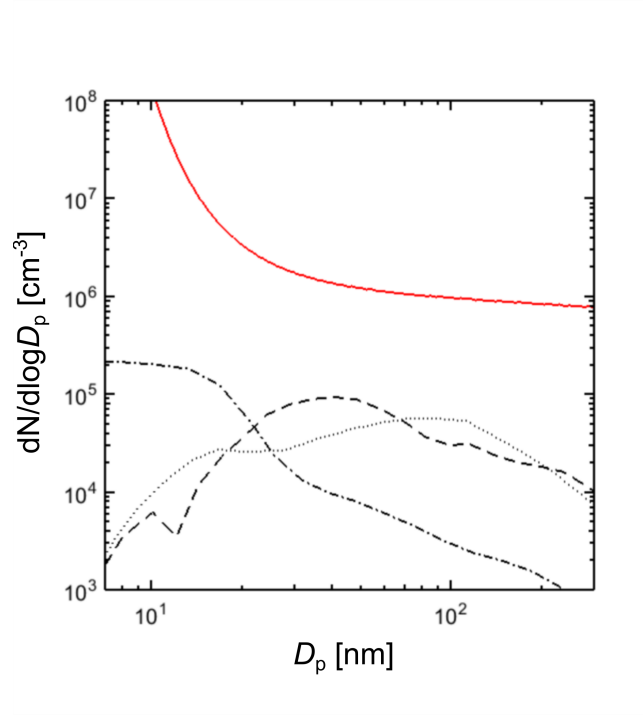


Figure S.4: Simulated maximum particle number size distribution with negligible impact of coincidence on WFIMS measurements (solid red line). Dotted [7], dashed [5] and dash-dotted [7] lines represent particle number size distributions measured in polluted urban environments.

distributions measured in polluted urban environments. Clearly $n_{\text{WFIMS}}(\log D_p)$ exceeds typical aerosol number size distributions under polluted conditions by at least an order of magnitude. Therefore, we expect optical coincidences have negligible impact on the WFIMS measurements of atmospheric aerosols.

WFIMS counting statistics for typical ambient particle size distribution is examined. The WFIMS size range is divided into 30 logarithmically spaced size bins having geometric mean bin diameters $\bar{D}_{p,i} = \sqrt{D_{p,i}^{\min} \cdot D_{p,i}^{\max}}$ and bin width $\Delta \ln D_{p,i} \approx 0.11477$, which will be the typical size resolution used to invert ambient WFIMS data. For each size bin, the uncertainty σ_c in particle counts C measured by WFIMS can be approximated, based on Poisson statistics, as $\sigma_c = \sqrt{C}$. Taking into account that (i) WFIMS detects charged particles only, (ii) some particles are lost during transport inside the inlet, and (iii) only a fraction of aerosol particles introduced into the separator are detected within the viewing window we estimate C_i as

$$C_i = \Delta t \cdot Q_a \cdot \eta_{\text{trans}}(\bar{D}_{p,i}) \cdot \eta_{\text{pen}}(\bar{D}_{p,i}) \cdot f(+1, \bar{D}_{p,i}) \left. \frac{dN}{d \ln D_p} \right|_{D_{p,i}} \Delta \ln D_{p,i}. \quad (\text{S.10})$$

The uncertainty range of measured size distribution is then derived from σ_c based on C_i calculated using Eq. S.10, and is presented in Fig. S.5 for typical remote continental aerosols. Reduced charging, penetration and transmission efficiencies lead to low counting statistics for measured size distributions below 15 nm, similar to traditional SMPS measurements. For the typical remote continental aerosol, the low counting statistics below 15 nm is also partially due to the relatively low particle concentration in this size range. The relative uncertainty of 1s measurements is less than 30% for particles between 15 nm and 280 nm in diameter, which dominate the overall number concentration. Increasing the WFIMS sampling time to 10 s yields improvement in counting statistics, i.e. uncertainty below 20% between 12 nm and 370 nm. In addition, uncertainties in total number concentration and mean particle diameter derived from size distribution measurements are around 6% for 1 s sampling time and about 2% for 10 s.

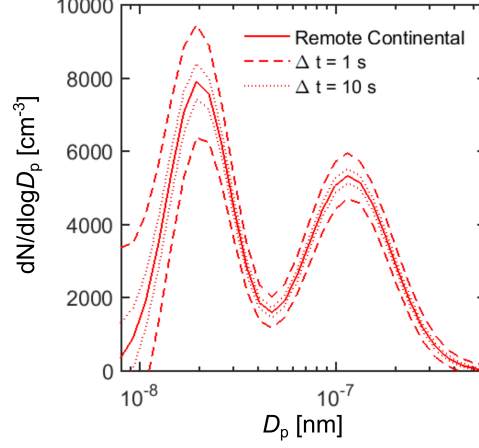


Figure S.5: Simulated counting statistics of WFIMS measurements for a typical remote continental aerosol. Solid lines represent size distributions of typical remote continental aerosol [2]. The uncertainty ranges of 1 s and 10 s measurements are shown by dashed and dotted lines, respectively.

S.6 WFIMS mobility resolution

For n_0 being the mobility distribution of singly charged particles introduced to a DMA, the WFIMS measurement of DMA classified particles is described by the response mobility distribution $n(Z_{p,DMA}, Z_p^*)$, which can be expressed as:

$$n(Z_{p,DMA}, Z_p^*) = \int \eta_{det}(Z'_p) \cdot p_{WFIMS}(Z'_p, Z_p^*) \cdot \eta_{pen}(Z'_p) \Omega(Z_{p,DMA}, Z'_p) \cdot n_0(Z'_p) dZ'_p. \quad (S.11)$$

$\eta_{pen}(Z'_p)$ and $\eta_{det}(Z'_p)$ are WFIMS penetration and detection efficiencies discussed in section 5.2. As shown in Fig. 8 η_{det} is about 1 for the entire particle size (mobility) range. The probability density distribution $p_{WFIMS}(Z'_p, Z_p^*)$ represents WFIMS transfer function. $p_{WFIMS}(Z'_p, Z_p^*) dZ'_p$ is the probability of measuring a particle of mobility Z'_p entering the separator within response mobility window $Z_p^* \rightarrow Z_p^* + dZ_p^*$. Note $p_{WFIMS}(Z'_p, Z_p^*) dZ'_p$ takes the restriction of the viewing window into account thus

$$\int p_{WFIMS}(Z'_p, Z_p^*) dZ'_p = \eta_{trans}(Z_p^*). \quad (S.12)$$

$\Omega(Z_{p,\text{DMA}}, Z'_p)$ is the probability of particles with mobility Z'_p leaving the DMA operated at classifying voltage V corresponding to centroid mobility $Z_{p,\text{DMA}}$. Typically $\Omega(Z_{p,\text{DMA}}, Z'_p)$ is a narrow function around $Z_{p,\text{DMA}}$. Thus Eq. S.11 can be simplified to

$$n(Z_{p,\text{DMA}}, Z_p^*) = \eta_{\text{det}}(Z_{p,\text{DMA}}) \cdot \eta_{\text{pen}}(Z_{p,\text{DMA}}) \cdot n_0(Z_{p,\text{DMA}}) \int p_{\text{WFIMS}}(Z'_p, Z_p^*) \cdot \Omega(Z_{p,\text{DMA}}, Z'_p) \cdot dZ'_p. \quad (\text{S.13})$$

assuming that η_{det} , η_{pen} and n_0 are relatively constant within the DMA mobility window.

Independent of the constant scaling factor $\eta_{\text{det}}(Z_{p,\text{DMA}}) \cdot \eta_{\text{pen}}(Z_{p,\text{DMA}}) \cdot n_0(Z_{p,\text{DMA}})$, the shape of measured/simulated response mobility distributions $n(Z_{p,\text{DMA}}, Z_p^*)$ is given by the integral in Eq. S.13, which we from now on refer to as $P^{\text{tot}}(Z_{p,\text{DMA}}, Z_p^*)$. The width of $P^{\text{tot}}(Z_{p,\text{DMA}}, Z_p^*)$ depends on both DMA and WFIMS mobility resolutions (Eq. S.13). As an analytic form of WFIMS transfer function is not available, it is very challenging to characterize the WFIMS transfer function experimentally through fitting a few controlling parameters as was done in [3]. Here we examine the WFIMS mobility resolution by comparing the measured and simulated response of WFIMS to monodispersed particles classified by a DMA. To facilitate the comparison, we first introduce the central response mobility \bar{Z}_p^* and overall mobility resolutions $R_{\text{FWHM}}^{\text{tot}}$ and $R_{\text{std}}^{\text{tot}}$ based on $P^{\text{tot}}(Z_{p,\text{DMA}}, Z_p^*)$.

The mean response mobility \bar{Z}_p^* can be written as

$$\bar{Z}_p^* = \frac{\int P^{\text{tot}}(Z_{p,\text{DMA}}, Z_p^*) Z_p^* dZ_p^*}{\int P^{\text{tot}}(Z_{p,\text{DMA}}, Z_p^*) dZ_p^*}. \quad (\text{S.14})$$

Typically \bar{Z}_p^* is close to $Z_{p,\text{DMA}}$, the DMA centroid mobility, and we write

$$R_{\text{FWHM}}^{\text{tot}}(Z_{p,\text{DMA}}) = \bar{Z}_p^* / \text{FWHM} \quad (\text{S.15})$$

and

$$\begin{aligned}
R_{\text{std}}^{\text{tot}}(Z_{\text{p,DMA}}) &= \bar{Z}_{\text{p}}^* / \sigma_{Z_{\text{p}}^*} \\
&= \bar{Z}_{\text{p}}^* \cdot \left[\frac{\int (Z_{\text{p}}^* - \bar{Z}_{\text{p}}^*)^2 \cdot P^{\text{tot}}(Z_{\text{p,DMA}}, Z_{\text{p}}^*) dZ_{\text{p}}^*}{\int P^{\text{tot}}(Z_{\text{p,DMA}}, Z_{\text{p}}^*) dZ_{\text{p}}^*} \right]^{-1/2}
\end{aligned}
\tag{S.16}$$

with $\sigma_{Z_{\text{p}}^*}$ being the standard deviation of $P^{\text{tot}}(Z_{\text{p,DMA}}, Z_{\text{p}}^*)$.

References

- [1] A. M. Collins, W. D. Dick, and F. J. Romy. A New Coincidence Correction Method for Condensation Particle Counters. *Aerosol Science and Technology*, 47(2):177–182, 2013.
- [2] R. Jaenicke. Tropospheric Aerosols. *International Geophysics*, 54:1–31, 1993.
- [3] P. Kulkarni and J. Wang. New fast integrated mobility spectrometer for real-time measurement of aerosol size distribution: II. Design, calibration, and performance characterization. *Journal of Aerosol Science*, 37:1326–1339, 2006.
- [4] K. W. Lee and J. A. Gieseke. Simplified calculation of aerosol penetration through channels and tubes. *Atmospheric Environment*, 14:1089–1094, 1980.
- [5] P. Mönkkönen, I. K. Koponen, K. E. J. Lehtinen, K. Hämeri, R. Uma, and M. Kulmala. Measurements in a highly polluted Asian mega city: observations of aerosol number size distribution, modal parameters and nucleation events. *Atmospheric Chemistry and Physics Discussions*, 4:5407–5431, 2004.
- [6] J. Wang. A fast integrated mobility spectrometer with wide dynamic size range: Theoretical analysis and numerical simulation. *Journal of Aerosol Science*, 40:890–906, 2009.
- [7] B. Wehner, A. Wiedensohler, T. M. Tuch, Z. J. Wu, M. Hu, J. Slanina, and C. S. Kiang. Variability of the aerosol number size distribution in Beijing, China: New particle formation, dust storms, and high continental background. *Geophysical Research Letters*, 31(22):1–4, 2004.

- [8] A. Wiedensohler. An approximation of the bipolar charge distribution for particles in the submicron size range. *Journal of Aerosol Science*, 19(3):387–389, 1988.
- [9] S.-H. Zhang and R. Flagan. Resolution of the radial differential mobility analyzer for ultrafine particles. *Journal of Aerosol Science*, 27:1179–1200, 1996.